

Quasi-thermal noise in a drifting plasma: Theory and application to solar wind diagnostic on Ulysses

Karine Issautier, Nicole Meyer-Vernet, Michel Moncuquet, and Sang Hoang

Département de Recherche Spatiale, Observatoire de Paris, Meudon, France

D. J. McComas

Los Alamos National Laboratory, Los Alamos, New Mexico

Abstract. The present paper provides the basic principles and analytic expressions of the quasi-thermal noise spectroscopy extended to measure the plasma bulk speed, as a tool for in situ space plasma diagnostics. This method is based on the analysis of the electrostatic field spectrum produced by the quasi-thermal fluctuations of the electrons and by the Doppler-shifted thermal fluctuations of the ions; it requires a sensitive radio receiver connected to an electric wire dipole antenna. Neglecting the plasma bulk speed, the technique has been routinely used in the low-speed solar wind, and it gives accurate measurements of the electron density and core temperature, in addition to estimates of parameters of the hot electron component. The present generalization of the method takes into account the plasma speed and thereby improves the thermal electron temperature diagnostic. The technique, which is relatively immune to spacecraft potential and photoelectron perturbations, is complementary to standard electrostatic analysers. Application to the radio receiver data from the Ulysses spacecraft yields an accurate plasma diagnostic. Comparisons of these results with those deduced from the particle analyser experiment on board Ulysses are presented and discussed.

1. Introduction

When a passive electric antenna is immersed in a stable plasma, the thermal motion of the ambient particles produces electrostatic fluctuations, which can be adequately measured with a sensitive wave receiver connected to a wire dipole antenna. This quasi-thermal noise (QTN) is completely determined by the particle velocity distributions in the frame of the antenna [Rostoker, 1961]. The problem is simplest in the absence of a static magnetic field or at frequencies much higher than the electron gyrofrequency, since in this case the plasma can be considered to be an assembly of "dressed" "test" particles moving in straight lines. The QTN spectrum around the plasma frequency f_p consists of a noise peak just above f_p produced by electron thermal fluctuations. Since the plasma density n_e is proportional to f_p^2 , this allows an accurate measurement of the electron density. In addition, the electrons passing within a Debye length L_D from the antenna induce voltage pulses on it, producing in the spectrum a plateau just below f_p , and above f_p , a noise level which decreases as the observing frequency increases. The analysis of these spectrum regions gives the electron core temperature T_c [Meyer-Vernet and Perche, 1989]. As pointed out by Meyer-Vernet *et al.* [1998], one of the main

advantages of the QTN spectroscopy is its relative immunity to the spacecraft potential and photoelectron perturbations which, in general, affect particle analysers.

This method, based on the electron contribution to the QTN, was first introduced for studies of the solar wind by Meyer-Vernet [1979]. It was applied successfully in cometary plasma tail [Meyer-Vernet *et al.*, 1986] and in magnetized planetary environments [Moncuquet *et al.*, 1995], and it was routinely used in the ecliptic plane to study the solar wind plasma at various heliocentric distances [Hoang *et al.*, 1992; Maksimovic *et al.*, 1995].

However, in addition to the electron thermal noise, the lower-frequency part of the QTN spectrum, first identified on ISEE 3 by Hoang *et al.* [1982] and interpreted quantitatively by Meyer-Vernet *et al.* [1986], is due to (1) the shot noise produced by particle impacts and photoemission on the antenna and (2) the ion thermal noise which is strongly Doppler-shifted by the solar wind velocity (so that it can be observed well above the ion characteristic frequencies). Since the proton and electron thermal velocities, v_{thp} and v_{the} , respectively, satisfy the inequality $v_{thp} \leq \mathbf{V} \leq v_{the}$ in the solar wind, the bulk velocity has essentially no effect on the electron thermal noise while it may significantly affect that of the ions [Issautier *et al.*, 1996].

In the present paper, we extend the QTN method to measure the solar wind speed by taking into account the proton thermal fluctuations which are Doppler-shifted by the plasma speed. This novel method is particularly necessary

Copyright 1999 by the American Geophysical Union.

Paper number 1998JA900165.

0148-0227/99/1998JA900165\$09.00

at high latitudes [Hoang *et al.*, 1996; Issautier *et al.*, 1998] where the wind speed is large, and hence significantly affects the plasma QTN.

In section 2 we briefly recall the theory of the QTN in a drifting electron-ion plasma and give the relevant analytical expressions; we introduce a simplifying assumption to deduce an easy-to-compute formula, and we give numerical results for the purpose of plasma diagnostics. In section 3 we apply our method to the radio receiver data on the Ulysses spacecraft, and we discuss the resulting uncertainties on the deduced plasma parameters. We then briefly compare, in section 4, our results with those given by the particle analyser on board Ulysses, and we discuss the observed discrepancies.

2. Quasi-Thermal Noise in a Drifting Plasma

2.1. Basics of the Method

The voltage spectral density measured at the terminals of an electric antenna, which is immersed in a plasma drifting with velocity \mathbf{V} , is

$$V_{\text{QTN}}^2(\omega) = \frac{2}{(2\pi)^3} \int d^3k \frac{|\mathbf{k} \cdot \mathbf{J}|^2}{k^2} E^2(\mathbf{k}, \omega - \mathbf{k} \cdot \mathbf{V}) \quad (1)$$

The first term in the integral represents the spatial Fourier transform $\mathbf{J}(\mathbf{k})$ of the current distribution on the antenna. For a wire dipole antenna made of two thin filaments, each of length L and radius $a \ll L$, parallel to the x axis, we have

$$\mathbf{k} \cdot \mathbf{J} = 4 \frac{\sin^2(k_x L/2)}{k_x L} \quad (2)$$

where we assume that the current has a linear variation (i.e., the charge distribution is constant on each antenna arm). This approximation holds, in general, whenever the filament radius is much smaller than the electrostatic wavelengths, i.e., $a \ll L_D$ and $\omega L/c \ll 1$ [Schiff, 1971].

The second term in the integral is the autocorrelation function of the electrostatic field fluctuations in the antenna frame. Since we consider frequencies much above the Larmor frequencies, so that the ambient static magnetic field can be neglected, we have

$$E^2(\mathbf{k}, \omega) = 2\pi \sum_i \frac{q_i^2 \int d^3v f_i(\mathbf{v}) \delta(\omega - \mathbf{k} \cdot \mathbf{v})}{\epsilon_0^2 k^2 |\epsilon_L(\mathbf{k}, \omega)|^2} \quad (3)$$

where f_i is the velocity distribution function of the i th species of charge q_i and $\epsilon_L(\mathbf{k}, \omega)$ is the plasma longitudinal dielectric function [Sitenko, 1967]. We consider a plasma made of several species i with density n_i , mass m_i , and Maxwellian distributions with temperature T_i , drifting with velocity \mathbf{V} . The permittivity is then given by

$$\begin{aligned} \epsilon_L(\mathbf{k}, \omega - \mathbf{k} \cdot \mathbf{V}) &= 1 + \frac{e^2}{k^2 \epsilon_0} \sum_i \frac{n_i}{k_B T_i} \\ &\times \left[1 - \Phi(z_i) + j\sqrt{\pi} z_i e^{-z_i^2} \right] \end{aligned} \quad (4)$$

$$z_i = \frac{\omega - \mathbf{k} \cdot \mathbf{V}}{k v_{thi}} \quad (5)$$

$$\Phi(z) = 2ze^{-z^2} \int_0^z e^{x^2} dx \quad (6)$$

where the thermal speed $v_{thi} = (2k_B T_i/m_i)^{1/2}$. Substituting (2) and (3) in the general expression (1), we obtain a three-dimensional integral which requires, in general, complex numerical calculations [Couturier *et al.*, 1983].

2.2. Proton Thermal Noise: Analytical Simplifications

The proton contribution to the voltage power spectrum given in (1), in cylindrical coordinates of axis parallel to \mathbf{V} , is

$$\begin{aligned} V_p^2(\omega) &= \frac{8}{\pi^2} \frac{ne^2}{\epsilon_0^2} \left(\frac{m_e}{2\pi k_B T_e} \right)^{1/2} \mu \int_0^{+\infty} \frac{dk}{k^3} \times \\ &\int_{-1}^{+1} \frac{du}{|\epsilon_L(\mathbf{k}, \omega - kVu)|^2} \exp[-\mu^2(\omega - kVu)^2/v_{the}^2 k^2] \\ &\times \int_0^{2\pi} d\varphi \frac{\sin^4(kL/2 \cos \gamma)}{(kL \cos \gamma)^2} \end{aligned} \quad (7)$$

where μ is the ratio between the electron and proton thermal speed, $u = \cos \theta$ where θ is the angle between \mathbf{k} and \mathbf{V} , and the angle γ is given by

$$\cos \gamma = u \cos \beta + \sqrt{1 - u^2} \sin \beta \cos \varphi \quad (8)$$

where β is the angle between \mathbf{V} and the antenna, and φ is the azimuthal angle of \mathbf{k} in a plane perpendicular to \mathbf{V} . In order to obtain a practical formula which can be used for a plasma diagnostic, we consider below the two simple cases where the antenna is perpendicular and parallel to the solar wind velocity \mathbf{V} , respectively.

It is worth noting that the first case is the most interesting in practice. First, with an antenna larger than the relevant wavelengths, which is generally the case for thermal noise diagnostics, the antenna is most sensitive to wave vectors roughly perpendicular to it [Meyer-Vernet, 1994]. Hence, since the effect of the velocity is maximum for \mathbf{k} parallel to \mathbf{V} , the proton contribution to the thermal noise (which increases with the Doppler shift) is expected to be maximum when the antenna is perpendicular to \mathbf{V} . Second, with a spinning antenna this geometry generally occurs twice per spin period.

In the particular case of Ulysses, the antenna is always approximately perpendicular (within 20°) to the velocity during most of the trajectory, since Ulysses's spin axis is close to the solar direction. Notice that a misalignment effect on the plasma diagnostic is estimated to be negligible since no detectable spin modulation has been observed in the spectra.

2.2.1. Antenna perpendicular to solar wind velocity. In this case, $\beta = \pi/2$, so that $\cos \gamma = \sqrt{1 - u^2} \cos \varphi$. The integration according to φ can be written as

$$I_\varphi = \int_0^{2\pi} d\varphi \frac{\sin^4(kL \cos \gamma/2)}{(kL \cos \gamma)^2} \quad (9)$$

$$I_\varphi = \frac{\pi}{16} F_\perp(kL\sqrt{1-u^2}) \quad (10)$$

$F_\perp(x)$ is the antenna response to a wave field having a cylindrical symmetry [Meyer-Vernet *et al.*, 1993]:

$$\begin{aligned} F_\perp(x) &= \frac{64}{\pi} \int_0^x ds \frac{\sin^4(s/2)}{s^2(x^2-s^2)^{1/2}} \\ &= \frac{8}{x} [2 \int_0^x dt J_0(t) - \int_0^{2x} dt J_0(t) \\ &\quad + J_1(2x) - 2J_1(x)] \end{aligned} \quad (11)$$

where J_0 and J_1 denote the Bessel functions of the first kind.

In (7) the exponential contributes most to the integral on the variable u near $u = \omega/kV$, within an interval of order v_{thp}/V ; otherwise, it is negligible. Since $V/v_{thp} \gg 1$, the variation of the function $F_\perp(x)$ is generally small over this interval (provided, in practice, that $L/L_D < V/v_{thp}$), and we can approximate the three-dimensional integral in (7) by

$$\begin{aligned} I_{k,u} &\approx \frac{\pi}{16} \int_{\omega/V}^{\infty} \frac{dk}{k^3} F_\perp\left(kL\sqrt{1-\frac{\omega^2}{k^2V^2}}\right) \times \\ &\int_{-1}^1 \frac{du}{|\epsilon_L(\mathbf{k}, \omega - kVu)|^2} \exp[-\mu^2(\omega - kVu)^2/k^2v_{the}^2] \end{aligned} \quad (12)$$

In an electron-proton plasma with Maxwellian distributions, the longitudinal dielectric function (4) can be written as

$$\begin{aligned} \epsilon_L(\mathbf{k}, \omega - kVu) &= 1 + \frac{1}{k^2L_D^2} [1 - \Phi(z) + j\sqrt{\pi}ze^{-z^2} \\ &\quad + t(1 - \Phi(\mu z) + j\sqrt{\pi}\mu ze^{-\mu^2z^2})] \end{aligned} \quad (13)$$

where t is the ratio of the electron to the proton temperature and $z = (\omega - kVu)/kv_{the}$. Equation (13) neglects the contribution to ϵ_L of the suprathermal component of the electron distribution. This is justified since the proton quasi-thermal noise (which we want to calculate) is only important below the plasma frequency; at these frequencies the electron suprathermal component contributes negligibly.

Let us denote the value of ϵ_L when the ion motion is neglected by ϵ_{L_e} , and the ion contribution by ϵ_{L_p} , so that

$$\epsilon_L = \epsilon_{L_e} + \epsilon_{L_p} \quad (14)$$

and

$$e^{-\mu^2z^2} = \frac{k^2L_D^2}{t\sqrt{\pi}\mu z} \Im[\epsilon_{L_p}] \quad (15)$$

where \Im denotes the imaginary part.

The integration over the variable u between -1 and 1 can be approximated by an integration between $-\infty$ and $+\infty$ because its main contribution occurs near $u = \omega/kV$, as said above. With the transformation $\omega' = \omega - kVu$, thus $\omega' = zk v_{the}$, the integral over u in (12) can be written as

$$I_u = \frac{k^2L_D^2}{t\mu M\sqrt{\pi}} \int_{-\infty}^{+\infty} \frac{d\omega'}{\omega' |\epsilon_L(\mathbf{k}, \omega')|^2} \quad (16)$$

where we have introduced the notation $M = V/v_{the}$.

Using (14), we have approximately

$$\begin{aligned} \int_{-\infty}^{+\infty} \frac{d\omega'}{\omega' |\epsilon_L(\mathbf{k}, \omega')|^2} &\approx \int_{-\infty}^{+\infty} \frac{d\omega'}{\omega' |\epsilon_L(\mathbf{k}, \omega')|^2} \\ &\quad - \int_{-\infty}^{+\infty} \frac{d\omega'}{\omega' |\epsilon_{L_e}(\mathbf{k}, \omega')|^2} \end{aligned} \quad (17)$$

where we have neglected the proton motion contribution to the modulus of the dielectric function in the second term of the right-hand side of (17), since $\mu z \gg 1$.

Since $\Im[\epsilon_L]/|\epsilon_L|^2 = \Im(1/\epsilon_L^*)$ (where $*$ denotes the complex conjugate), and using the Kramers-Kronig relations as explained in the Appendix (see equation (A8)), (17) can be written as

$$\begin{aligned} \int_{-\infty}^{+\infty} \frac{d\omega'}{\omega' |\epsilon_L(\mathbf{k}, \omega')|^2} &\approx \pi \Re \left[1 - \frac{1}{\epsilon_L(\mathbf{k}, 0)} \right] \\ &\quad - \pi \Re \left[1 - \frac{1}{\epsilon_{L_e}(\mathbf{k}, 0)} \right] \end{aligned} \quad (18)$$

where

$$\epsilon_L(\mathbf{k}, 0) = 1 + \frac{1}{k^2L_D^2}(1+t) \quad (19)$$

$$\epsilon_{L_e}(\mathbf{k}, 0) = 1 + \frac{1}{k^2L_D^2} \quad (20)$$

Hence, substituting (18) into (16), we finally obtain

$$I_u = \frac{(kL_D)^4}{t\mu M} \sqrt{\pi} \left[\frac{1}{1+k^2L_D^2} - \frac{1}{1+t+k^2L_D^2} \right] \quad (21)$$

Substituting (12) into (7), using (21) and making a change of variables in the integral, the proton thermal noise takes the simple expression [Issautier *et al.*, 1996]

$$\begin{aligned} V_p^2(\omega) &= \frac{(2m_e k_B)^{1/2} \sqrt{T_e}}{4\pi\epsilon_0 M} \int_0^\infty dy \\ &\quad \times \frac{y F_\perp(yL/L_D)}{(y^2+1+\Omega^2)(y^2+1+\Omega^2+t)} \end{aligned} \quad (22)$$

$$\Omega = \omega L_D/V, \quad t = T_e/T_p, \quad M = V/v_{the} \quad (23)$$

As previously said in section 2.2.1, the function F_\perp is the antenna response to the wave field. The electron Debye length L_D is defined by $L_D^2 = (\epsilon_0 k_B T_e / e^2 n_e)$, where n_e is the electron density and T_e is a generalized electron temperature defined by $k_B T_e / m_e = 1 / \langle v^{-2} \rangle$ (where $\langle \rangle$ denotes an average over the electron velocity distribution). With a Maxwellian distribution of temperature T , we get the usual definition $T_e = T$ instead of $T_e = T_c(1+\alpha)/(1+\alpha\tau^{-1})$ with a superposition of a cold plus a hot Maxwellian, where $\alpha = n_h/n_c$ and $\tau = T_h/T_c$. With $\alpha \ll 1$ and $\tau \gg 1$ in the solar wind [Feldman *et al.*, 1975], the temperature T_e is roughly equal to the core electron temperature T_c .

2.2.2. Antenna parallel to solar wind velocity. In this limiting case, we can also deduce an expression of the proton

thermal noise $V_p(\omega)$, that is easy to compute. With $\beta = 0$, (8) yields $\cos \gamma = \cos \theta = u$, so that the proton thermal noise expression becomes

$$V_p^2(\omega) = \frac{16 n e^2}{\pi \epsilon_0^2} \left(\frac{m_e}{2\pi k_B T_e} \right)^{1/2} \mu \int_0^{+\infty} \frac{dk}{k^3} \times \int_{-1}^{+1} du \frac{\sin^4(kLu/2)}{(kLu)^2} \frac{1}{|\epsilon_L(\mathbf{k}, \omega - kVu)|^2} \times \exp[-\mu^2(\omega - kVu)^2/v_{the}^2 k^2] \quad (24)$$

where the permittivity function is given by (13). As said in section 2.2.1, the exponential function contributes mostly to the integral in the vicinity of $u = \omega/kV$. Thus we can approximate (24) by

$$V_p^2(\omega) \propto \frac{\sin^4(L\omega/2V)}{(L\omega/V)^2} \int_{\omega/V}^{+\infty} \frac{dk}{k^3} \times \int_{-1}^{+1} \frac{du}{|\epsilon_L(\mathbf{k}, \omega - kVu)|^2} \exp[-\mu^2(\omega - kVu)^2/v_{the}^2 k^2] \quad (25)$$

As previously shown in section 2.2.1, the integration over u can be calculated using the Kramers-Kronig relations, giving (21). Hence (25) yields

$$V_p^2(\omega) = \frac{16 T_p}{\pi n e^2} \frac{k_B^2 T_e}{V} \frac{\sin^4(L\omega/2V)}{(L\omega/V)^2} \times \int_{\omega/V}^{+\infty} \left[\frac{kdk}{1+k^2 L_D^2} - \frac{kdk}{1+t+k^2 L_D^2} \right] \quad (26)$$

where $t = T_e/T_p$. This can be straightforwardly integrated to give the expression of the proton thermal noise when the antenna is parallel to the velocity

$$V_p^2(\omega) = \frac{8k_B T_e}{\pi \epsilon_0 V t} \frac{\sin^4(a\Omega/2)}{(a\Omega)^2} \ln \left[\frac{1+t+\Omega^2}{1+\Omega^2} \right] \quad (27)$$

where $\Omega = \omega L_D/V$ and $a = L/L_D$. It is important to note that the approximation used to obtain (25) assumes that the sine function in (24) varies weakly when u varies by v_{thp}/V , i.e., in practice that $4L/L_D < V/v_{thp}$, which is a stronger condition than that assumed to derive (22) in the case of an antenna perpendicular to \mathbf{V} .

2.3. Asymptotic Limits and Numerical Results

2.3.1. Asymptotic limits. The proton thermal noise, when the velocity is perpendicular to the antenna, can be simplified in the following asymptotic limits. Consider first the case $L/L_D \gg 1$. Substituting the asymptotic limit $F_{\perp}(\mathbf{x}) \sim 8/x$ for $x \gg 1$ [Meyer-Vernet *et al.*, 1993] into (22), we obtain

$$V_p^2 \approx \frac{4k_B T_e}{\pi \epsilon_0 V} \frac{1}{at} \int_0^{\infty} dy \times \left[\frac{1}{1+\Omega^2+y^2} - \frac{1}{1+\Omega^2+y^2+t} \right] \quad (28)$$

This can be straightforwardly integrated to give

$$V_p^2 \approx \frac{2k_B T_e}{\epsilon_0 V} \frac{L_D}{Lt} \left[\frac{1}{\sqrt{1+\Omega^2}} - \frac{1}{\sqrt{1+\Omega^2+t}} \right] \quad (29)$$

It is worth noting that in the special case when $t \ll 1 + \Omega^2$, (29) reduces to

$$V_p^2 \approx \frac{k_B T_e}{\epsilon_0 V} \frac{L_D}{L} \frac{1}{(1+\Omega^2)^{3/2}} \quad (30)$$

which is independent of the electron to proton temperature ratio.

Consider now the case $L/L_D \ll 1$. We substitute the approximation $F_{\perp}(\mathbf{x}) \sim x^2$ for $x \ll 1$ [Meyer-Vernet *et al.*, 1993] into (22), which yields

$$V_p^2 \approx \frac{k_B T_e}{2\pi \epsilon_0 V} \frac{a^2}{t} \int_0^{1/a} dy \times \left[\frac{y^3}{1+\Omega^2+y^2} - \frac{y^3}{1+\Omega^2+y^2+t} \right] \quad (31)$$

since the large values of y contribute negligibly to the integral. Finally, we obtain

$$V_p^2 \approx \frac{k_B T_e}{4\pi \epsilon_0 V} \frac{L^2}{L_D^2 t} \times \left[(1+\Omega^2+t) \ln \left(1 + \frac{L_D^2}{L^2(1+\Omega^2+t)} \right) - (1+\Omega^2) \ln \left(1 + \frac{L_D^2}{L^2(1+\Omega^2)} \right) \right] \quad (32)$$

In particular, when $t \ll 1 + \Omega^2$, this gives

$$V_p^2 \approx \frac{k_B T_e}{4\pi \epsilon_0 V} \frac{L^2}{L_D^2} \ln \frac{L_D^2}{L^2(1+\Omega^2)} \quad (33)$$

2.3.2. Numerical results. Figure 1 shows the proton thermal noise spectra normalized to $\sqrt{T_e}$ for the slow and fast wind speed versus the normalized frequency f/f_p . For each case, the parameter L/L_D varies between 0.5 and 10 as shown in Figure 1 by different styles of lines. We have also used $f_p = 15$ kHz, $T_e = 10^5$ K, and $T_p = 5 \times 10^4$ K. For the lower value of the solar wind speed, the proton noise is more intense at low frequencies ($f < f_p$) than it is in the case of large-speed wind. Besides, the signal decreases more rapidly with the frequency for $V = 400$ km s⁻¹ than for $V = 800$ km s⁻¹. In the latter case, the noise is shifted to larger frequencies. The larger the wind speed, the more shifted the proton noise.

Figure 2 represents the most general grid of spectra of the proton thermal noise normalized to $\sqrt{T_e}/M$ as a function of $f/(f_p M)$. The curves depend only on two parameters: the antenna length normalized to the Debye length and the ratio of the electron to proton temperature. For two cases of electron to proton temperature ratio, $t = 0.5$ and $t = 2$, we draw the proton noise spectra, deduced from (22) for different values of L/L_D . Figure 2 can be used for any kind of wind, knowing the characteristic of the plasma and the length of the antenna. When the wind speed is changed, the proton noise spectrum is shifted in both frequency and amplitude according to the value of M .

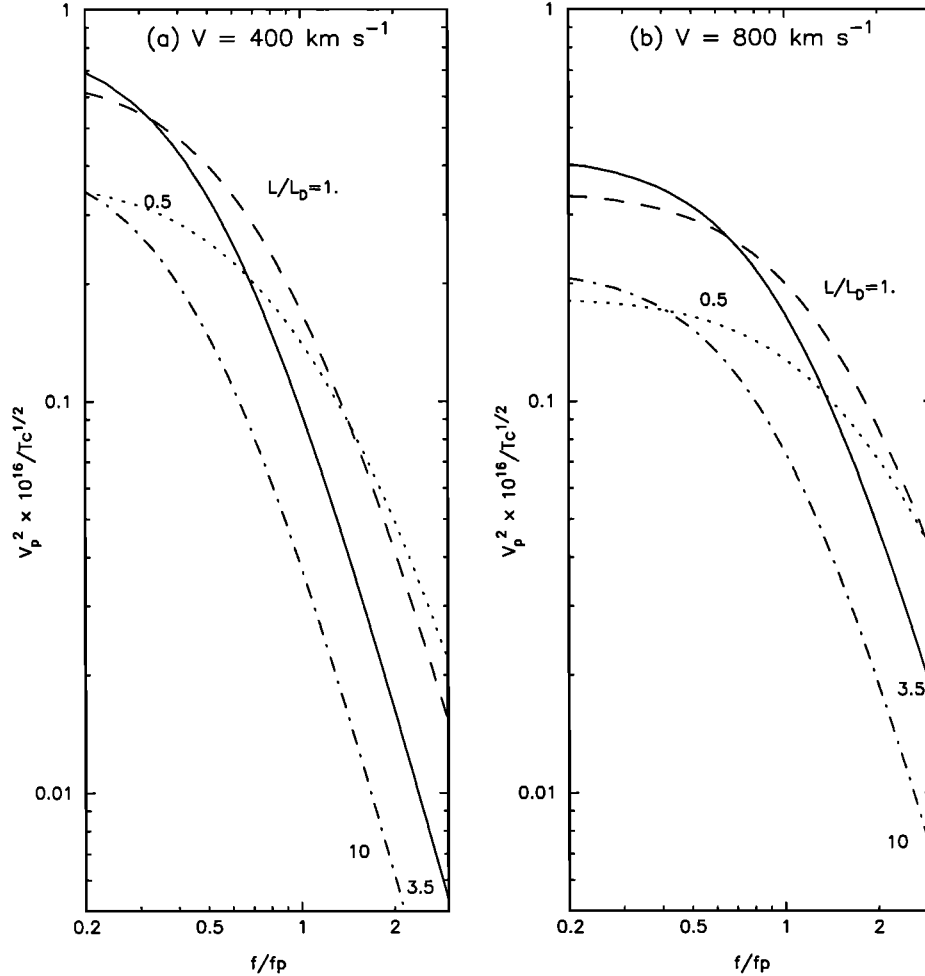


Figure 1. Proton thermal noise level $V_p^2 (V^2 \text{ Hz}^{-1}) \times 10^{16}/T_c^{1/2}$ (K) as a function of f/f_p for a wire dipole antenna with different values of L/L_D (0.5, 1, 3.5, and 10), for (a) the low speed wind and (b) the fast speed wind. As an example, we take $f_p = 15$ kHz, $T_p = 5 \times 10^4$ K, and $T_c = 10^5$ K.

Figure 3 shows the contour levels of the proton thermal noise at $f/f_p = 0.5$ as a function of the electron density and core temperature for the Ulysses wire dipole antenna with length $L = 35$ m, for wind speeds of 400 and 800 km s^{-1} , and $T_p = 8 \times 10^4$ K. Since the density only plays a role through L/L_D in (22), it scales as L^{-2} , so that one can use this chart with any antenna length: for instance, if $L = 70$ m, then the density n_e in Figure 3 must be divided by 4. The dotted line corresponds to the plasma parameters for which $L/L_D = 1$. It is noteworthy that Figure 3 may be used for comparison with Figure 4 of Meyer-Vernet and Perche [1989]. The dashed line is the condition where $L/L_D = \mu M$. The proton thermal noise calculations performed in this paper assume that $L/L_D < \mu M$ (as discussed in section 2.2.1), which is given by the large region above the dashed line.

2.4. Electron Diagnostic

2.4.1. Electron thermal noise. The electron thermal noise, reviewed by Meyer-Vernet and Perche [1989], is deduced from the expression (1) of the voltage spectrum where

the Doppler shift on the electrons is generally negligible since $V \ll v_{the}$, so that it can be calculated numerically from a simple one-dimensional integral. For a wire dipole antenna the electron QTN spectrum is nearly flat just below the plasma frequency, at a level mainly determined by the core temperature T_c . In contrast, when $f \gg f_p$, the electron quasi-thermal noise is given by Meyer-Vernet and Perche [1989]:

$$V_e^2 \sim 5 \cdot 10^{-16} \sqrt{T_c} \frac{L_D c}{L} \times 1.6 \frac{f_p^3 (1 + \alpha \tau)}{f^3 (1 + \alpha)^{3/2}} \quad (34)$$

for two Maxwellian electron populations with $\alpha = n_h/n_c$ and $\tau = T_h/T_c$.

The electron noise spectrum has a cutoff at the plasma frequency $f_p \propto (n_c + n_h)^{1/2}$ and a peak just above f_p whose precise shape is determined by the halo population, through the parameters α and τ . Notice that when $f \gg f_p$, V_e^2 varies as $1/f^3$, whereas one can see from expression (22) that for high frequencies the proton thermal noise varies as $1/f^4$. Hence the proton thermal noise tends to be negligible above f_p , whereas the electron thermal noise dominates. In con-

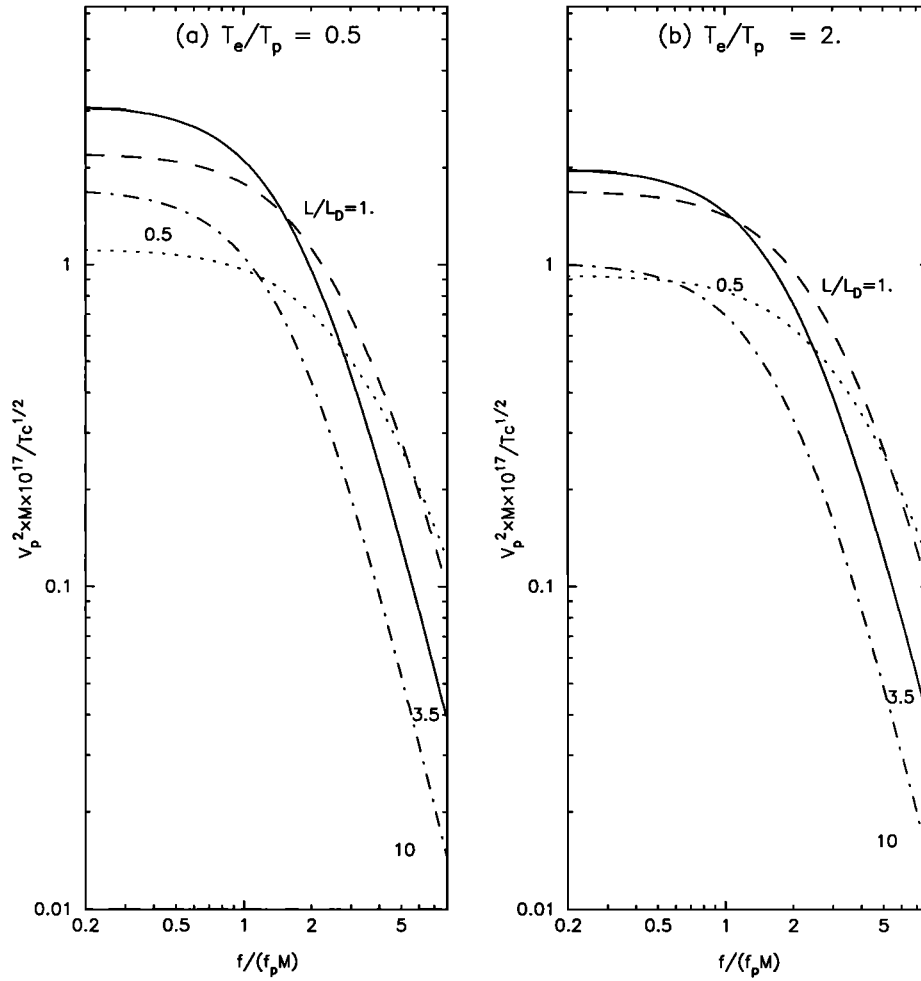


Figure 2. Chart plots of the normalized proton thermal noise level $V_p^2 (V^2 \text{ Hz}^{-1}) \times 10^{17} \times M/T_c^{1/2}$ (K) as a function of $f/(f_p M)$ for different values of L/L_D as shown and for (a) $t = 0.5$ and (b) $t = 2$.

trast, one can see, by comparing Figures 1-3 with those of Meyer-Vernet and Perche [1989], that the proton noise plays an important role below the plasma frequency.

2.4.2. Solar wind speed effect on the plasma frequency cutoff. In a Maxwellian electron plasma described by the Vlasov equation, the dispersion equation of the weakly damped longitudinal plasma waves is defined by the real part of the dielectric function ϵ_L given by (4). With a relative velocity \mathbf{V} of the antenna with respect to the ambient plasma, the dispersion relation is then

$$\Re[\epsilon_L(\mathbf{k}, \omega - \mathbf{k} \cdot \mathbf{V})] = 0 \tag{35}$$

Expanding the dielectric function in terms of small parameter $k^2 \langle v^2 \rangle / \omega^2$, we obtain

$$(\omega - \mathbf{k} \cdot \mathbf{V})^2 \approx \omega_p^2 \left(1 + \frac{k^2 \langle v^2 \rangle}{(\omega - \mathbf{k} \cdot \mathbf{V})^2} \right) \tag{36}$$

where $\langle v^2 \rangle$ is the second order moment of the distribution function, which traditionally defines the temperature. With the notation $\mathbf{k} \cdot \mathbf{V} = kVu$, we have

$$\frac{\omega^2}{\omega_p^2} \left(1 - \frac{2kVu}{\omega} \right) \approx 1 + \frac{k^2 \langle v^2 \rangle}{\omega^2} \tag{37}$$

This second degree polynomial in k^2 has two solutions defined by

$$k = \frac{\omega^2}{\langle v^2 \rangle} \left[-\frac{\omega Vu}{\omega_p^2} \pm \sqrt{\left(\frac{\omega Vu}{\omega_p^2} \right)^2 - \frac{\langle v^2 \rangle}{\omega^2} \left(1 - \frac{\omega^2}{\omega_p^2} \right)} \right] \tag{38}$$

Since k is real and positive, there is always one solution (obtained by taking the positive sign) whatever the sign of u if $\omega \geq \omega_p$; this is the usual Langmuir wave Doppler-shifted by the velocity \mathbf{V} . In contrast, for $\omega < \omega_p$ the existence of a solution (obtained by taking the negative sign) requires that $u < 0$ and

$$\left(\frac{\omega Vu}{\omega_p^2} \right)^2 \geq \frac{\langle v^2 \rangle}{\omega^2} \left(1 - \frac{\omega^2}{\omega_p^2} \right) \tag{39}$$

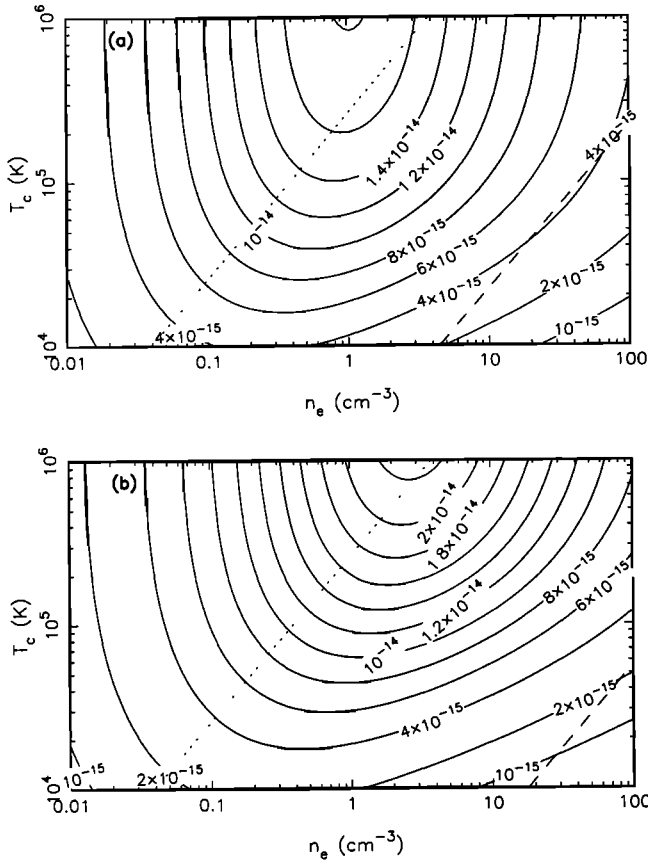


Figure 3. Proton thermal noise contours (V_p^2 in $V^2 \text{ Hz}^{-1}$) for $f/f_p = 0.5$ as a function of the plasma density and temperature, for a thin dipole antenna with $L = 35$ m and $T_p = 8 \times 10^4$ K for two wind speeds of (a) $V = 400 \text{ km s}^{-1}$ and (b) $V = 800 \text{ km s}^{-1}$. All contour levels are in the range between 10^{-15} and 2.6×10^{-14} and are spaced as follows: for example, the proton noise contours (in $10^{-15} V^2 \text{ Hz}^{-1}$) are 1, 2, 4, 6, 8, 10, 12, 14, 16, 18, 20, and 22.

For $\omega \approx \omega_p$ this can be rewritten as

$$1 - \frac{\omega^2}{\omega_p^2} < \frac{u^2 V^2}{\langle v^2 \rangle} \quad (40)$$

Hence the Doppler shift allows weakly damped waves to exist even below the plasma frequency, in the range

$$\omega \geq \omega_p \left(1 - \frac{V^2 u^2}{2 \langle v^2 \rangle} \right) \quad (41)$$

Since $u \leq 1$, we conclude that electrostatic waves are detected by the antenna below f_p owing to the Doppler shift, for frequencies as low as $f_p (1 - V^2/2 < v^2 >)$. The cutoff of the spectrum, which is located at the plasma frequency for $V = 0$, is therefore shifted to the left, which may widen the peak.

For a typical speed wind of about 400 km s^{-1} , and an electron temperature $T_e \sim 10^5$ K, the ratio $V^2 / \langle v^2 \rangle$ is small. We get $V/v_{the} \sim 0.23$ with a three-dimensional Maxwellian distribution which gives $\langle v^2 \rangle = 3k_B T_e / m_e =$

$3/2 v_{the}^2$, so that the cutoff is determined with a maximum error of 2%, due to the Doppler shift effect.

In contrast, at high latitudes where the solar wind speed is large, for $V \sim 800 \text{ km s}^{-1}$ and $T_e \sim 7 \times 10^4$ K, V/v_{the} is about 0.6. In this case the cutoff is shifted by 10% toward the left of the spectrum, so that the Doppler shift effect on the plasma frequency is still small but not negligible.

3. Solar Wind Plasma Diagnostic

3.1. Shot Noise and Antenna Impedance

Since the wire dipole antenna used is not a grid antenna, there is an additional noise due to the particles whose trajectory intercepts the antenna and also to the photoelectrons which are emitted by the antenna surface. This shot noise becomes important only for $f \ll f_p$ and decreases as $1/f^2$. Although it is generally small for the antenna used, we have to take it into account to make an accurate plasma diagnostic. If the DC potential ϕ and the equivalent radius a of the antenna satisfy $|e\phi/k_B T| \ll 1$ and $a < L_D$, the electron impact rate on one antenna arm is roughly $N_e \approx \sqrt{\pi} a L n_e v_{the}$. A good approximation for the total noise at the antenna terminals below f_p can be obtained by simply adding to the electron-plus-ion QTN the term representing the shot noise [Meyer-Vernet and Perche, 1989],

$$V_I^2 = 2e^2 N_e A |Z|^2 \quad (42)$$

where the factor $A \approx 1 + e\phi/k_B T_e$ comes from a first-order approximation of the shot noise (ϕ is estimated to be ~ 4 V) and Z is the antenna impedance, defined by

$$Z(\omega) = \frac{j}{(2\pi)^3 \epsilon_0 \omega} \int d^3 k \frac{|\mathbf{k} \cdot \mathbf{J}(\mathbf{k})|^2}{k^2 \epsilon_L(\mathbf{k}, \omega - \mathbf{k} \cdot \mathbf{V})} \quad (43)$$

which takes into account the effect of the ambient plasma. Note that the uncertainty on the determination of ϕ does not affect significantly our results because we only take into account the data for which the shot noise contribution V_I^2 to the total noise is very small (see section 3.5).

The terminals of the antenna, of impedance Z , are connected through an input circuit to a receiver with a finite input impedance Z_R ; then the voltage spectral density measured at the receiver input terminals is $V_R^2 = V_\omega^2 / \Gamma^2$, where the total quasi-thermal noise V_ω^2 is the sum of $V_p^2(\omega)$, $V_e^2(\omega)$, and $V_I^2(\omega)$, given by expressions (22), (34), and (42), respectively. The transfer function of the input circuit is defined as a function of the impedances by

$$\frac{1}{\Gamma^2} = \left| \frac{Z_R}{Z_R + Z} \right|^2 \quad (44)$$

where Z_R is mainly due to the antenna base capacitance.

3.2. Unified Radio and Plasma Wave Receiver

The observations were performed with the Unified Radio and Plasma Wave (URAP) radio receiver [Stone et al., 1992], connected to the long wire 2×35 m electric dipole

antenna, located in the spacecraft spin plane. The receiver is linearly swept through 64 equally spaced and contiguous frequency channels (of bandwidth 0.75 kHz and duration 2 s), covering the low-frequency band from 1.25 to 48.5 kHz in 128 s. This receiving mode is well suited to measure thermal noise spectra on Ulysses with a good frequency resolution. Besides, as we will see in section 3.5, the receiver is extremely sensitive, and the ratio of the signal to receiver noise is higher than in most previously flown instruments, which enables us to analyze accurately the plasma thermal noise.

3.3. Deducing the Bulk Speed

As said in section 2.2, because the proton thermal velocity is much smaller than the plasma bulk velocity, the proton noise spectrum is strongly Doppler-shifted, and it can be observed far above the proton characteristic frequencies. The solar wind speed is thus deduced from the analysis of the proton contribution to the low-frequency thermal spectrum.

As already noted, over most of the Ulysses trajectory, the spin axis is sufficiently close to the solar direction for the antenna to be roughly perpendicular to the solar wind velocity. We will then use the proton thermal noise expression given in (22).

We assume that the electron velocity distribution in the solar wind is a superposition of two isotropic Maxwellians; we model them by a core (of density n_c and temperature T_c) and a halo (of density n_h and temperature T_h) [Feldman *et al.*, 1975]. Moreover, we describe the proton distribution by one drifting Maxwellian (of speed V and temperature T_p). Although the electron halo population is often observed to be highly non-Maxwellian [see, e.g., Maksimovic *et al.*, 1997], this does not affect significantly the diagnostic of the total electron density, which is model independent, nor the core temperature, quite insensitive to the shape of the hot population distribution [Chateau and Meyer-Vernet, 1991]. However, it is not the case for suprathermal parameters.

Practically, the plasma diagnostic is performed by (1) assuming the above velocity distributions, (2) calculating the theoretical spectrum V_R^2 produced by these distributions, and (3) deducing the six unknown parameters of the model by fitting the theory to the whole measured spectrum, using a nonlinear least squares fitting procedure, as explained in section 3.4.

3.4. Numerical Process

The numerical process basically consists of fitting the theoretical voltage spectral density $\log V_R^2$ to each measured spectrum by minimizing a χ^2 merit function with the six free following parameters: the plasma frequency f_p , the core temperature T_c , the ratio of the halo/core densities $\alpha = n_h/n_c$, the ratio of the halo/core temperatures $\tau = T_h/T_c$, the ion solar wind speed V , and the proton temperature T_p . These χ^2 minima are found by using a Levenberg-Marquart method [Press *et al.*, 1992], which also provides the estimated variances of the fitted parameters, used herein to deduce their uncertainties. The χ^2 function is computed by using equal measurement errors of about 10% on the measured

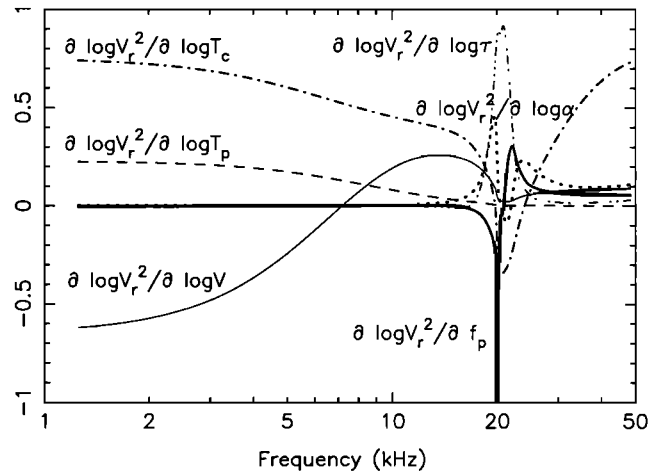


Figure 4. Partial derivatives of the electron-plus-proton quasi-thermal noise spectrum with respect to the six parameters of the fitting f_p , T_c , α , τ , V , and T_p , for typical values encountered by Ulysses (20 kHz, 7.5×10^4 K, 0.03, 13, 400 km s⁻¹ and 7×10^4 K respectively).

spectral density to weight the fitting; notice that this value is lower than the 15% previously used by Maksimovic *et al.* [1995], which has subsequently been found to be overestimated [Issautier *et al.*, 1998].

The implementation of the Levenberg-Marquart method requires computing the partial derivatives of the calculated QTN spectrum with respect to the six fitting parameters. Figure 4 shows these partial derivatives of the electron-plus-proton thermal noise for typical solar wind parameters. This allows us to provide the sensitivity of the QTN spectrum to each parameter in the Ulysses frequency range. These derivatives are given with respect to the parameter decimal logarithm (except for f_p), so that a value of ± 1 at a given frequency means that multiplying or dividing the considered parameter by 10 (or adding or subtracting 1 kHz to f_p) multiplies or divides the QTN level by 10.

In Figure 4 one can see the following:

1. The thermal temperature is the only parameter which depends significantly on the whole spectrum (dash-dotted line). Compared to the QTN spectroscopy performed previously [see, e.g. Maksimovic *et al.*, 1995] for which the Doppler-shifted proton thermal noise was not included, the spectrum below f_p is now correctly calculated, which might allow us to measure T_c even when the spectrum above f_p is polluted by nonthermal emissions (such as type III radio bursts).

2. The derivative with respect to f_p exhibits a large variation but in a narrow frequency range around f_p (bold solid line); this is because it mainly depends on the voltage peak. Otherwise stated, the peak is a strong marker of the plasma frequency, which might allow one to determine f_p on a spectrogram by "fitting by eye."

3. For the suprathermal electron parameters the partial derivatives $\partial \log V_R^2 / \partial \log \alpha$ (dotted line) and $\partial \log V_R^2 / \partial \log \tau$ (dash-dotted line with three dots) also vanish outside

the vicinity of the peak and reach smaller values than $\partial \log V_R^2 / \partial f_p$ does (despite they are in logarithmic scale); this explains why these parameters are revealed by the detailed shape of the spectral peak as already shown by *Chateau and Meyer-Vernet* [1991] and why they are not very well determined by the fitting.

4. The partial derivative with respect to the logarithm of the solar wind speed (thin solid line) varies greatly (roughly speaking, as much as the derivative with respect to $\log T_c$) at frequencies below f_p , while this derivative vanishes above f_p , where the effect of the speed can thus be considered as negligible. As already shown by *Issautier et al.* [1996], the proton thermal noise is much more sensitive to the bulk speed than to the proton temperature, since the derivative with respect to T_p (dashed line) is significantly smaller than with respect to V . Moreover, the maximum values of $\partial \log V_R^2 / \partial \log T_p$ are obtained at very low frequencies where the shot noise dominates the spectrum. Note also that in (22) the solar wind speed V appears not only in the integral of the expression but also as a factor, so that the speed is determined by both the level of the proton noise and the spectral shape. In contrast, the proton temperature appears only through the parameter t in the integral. This is why the method is not well adapted to determine T_p , albeit it has no incidence on the speed diagnostic.

3.5. Applications on Ulysses

Routinely used on Ulysses, the method in section 3.4 yields for each spectrum the six plasma parameters (n_e , T_c ,

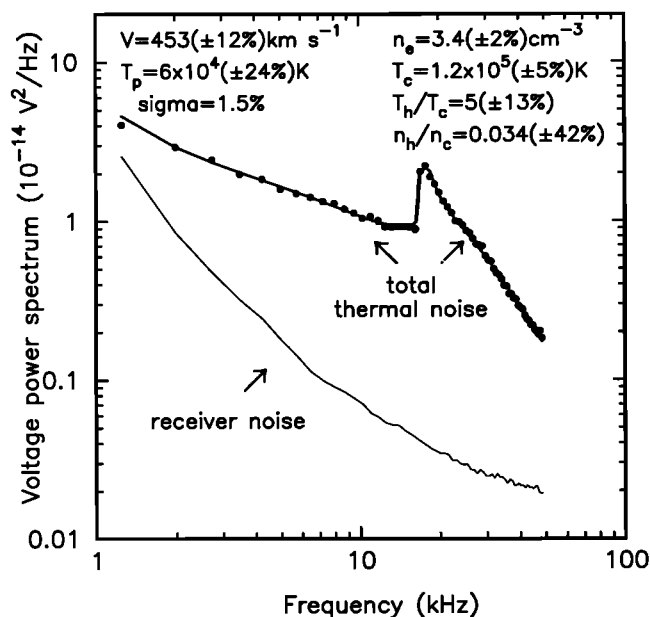


Figure 5. Example of voltage power spectrum (in $10^{-14} V^2 \text{ Hz}^{-1}$) measured with the Unified Radio and Plasma Wave (URAP) dipole antenna on Ulysses at 1.34 AU heliocentric distance. The bold solid line is the theoretical spectrum of the electron-plus-proton quasi-thermal noise (plus shot noise) which best fits the data (dots), with the plasma parameters shown, while the thin solid line represents the receiver noise level on Ulysses.

α , τ , V , and T_p), their numerical uncertainties, and the overall standard deviation σ of the theory from the data. This latter parameter quantifies the quality of the fit and allows us to select the best spectra. Note that in all Ulysses data analysis we required it to be better than 2.5%.

Figure 5 shows a typical example of the observed voltage power spectrum versus frequency. The bold solid line represents the best fit of the theoretical electron-plus-proton QTN (plus the shot noise at lowest frequencies) to the observed spectrum plotted as heavy dots. It is noteworthy that the numerical process involves fitting the model to many more independent data points (56 dots in the above example) than the number of free parameters (six). The fit is good since the σ is less than 2%. The thin solid line represents the receiver noise level against the frequency. This level, which decreases as the frequency increases, is always lower than $10^{-14} V^2 \text{ Hz}^{-1}$ except for the first frequency at 1.25 kHz; thus, the signal to the receiver noise ratio is generally higher than 10 above 5 kHz and remains at about 5 at lower frequencies. Hence we do not take into account, in the fitting procedure, the two lowest frequencies of the spectrum, for which the thermal noise is not sufficiently large compared with the receiver noise level and to the shot noise.

The fitting yields finally the six plasma parameters, with their uncertainties, shown in Figure 5; the best fitted parameters are, in the decreasing accuracy order, n_e , T_c , and V . Note that improving the statistical uncertainties on the suprathermal parameters would require a better frequency resolution of the spectral peak than that achieved on Ulysses since, as explained before, suprathermal particles are only revealed by the shape of the peak.

Figure 6 represents several typical examples of spectra routinely obtained with the Ulysses low-frequency receiver. As in Figure 5, the solid lines are the best fit spectra with the parameters shown. These spectra are taken at different latitudes during the Ulysses pole-to-pole exploration. This outlines the typical spectral shape, corresponding to specific types of wind (slow or fast wind and dense or dilute flows) encountered by the spacecraft; one can see, in particular, that the spectral peak is smoothed out at increasing latitudes, which is due in part to the increase of the Debye length due to the density decrease as the heliocentric distance increases [*Hoang et al.*, 1996]. Besides, we can verify from Figures 6c and 6f that the relative contribution α of the suprathermal particles to the density affects essentially the width of the peak.

The evolution of the statistical uncertainties of the plasma parameters, deduced from the fitting procedure, indicates that all of them depend, more or less, on the heliographic latitude. As the spacecraft explored the high latitudes where it encountered the steady state fast solar wind originating from polar coronal holes, the numerical errors increase (not shown). In particular, as already noted, the electron density is low in these polar regions, so that the f_p peak is shifted to lower frequencies near the lowest frequency of the receiver band, and the corresponding Debye length increase smooths out the peak. Both effects act to increase the uncertainty on the electron density. In addition, at high latitudes the solar

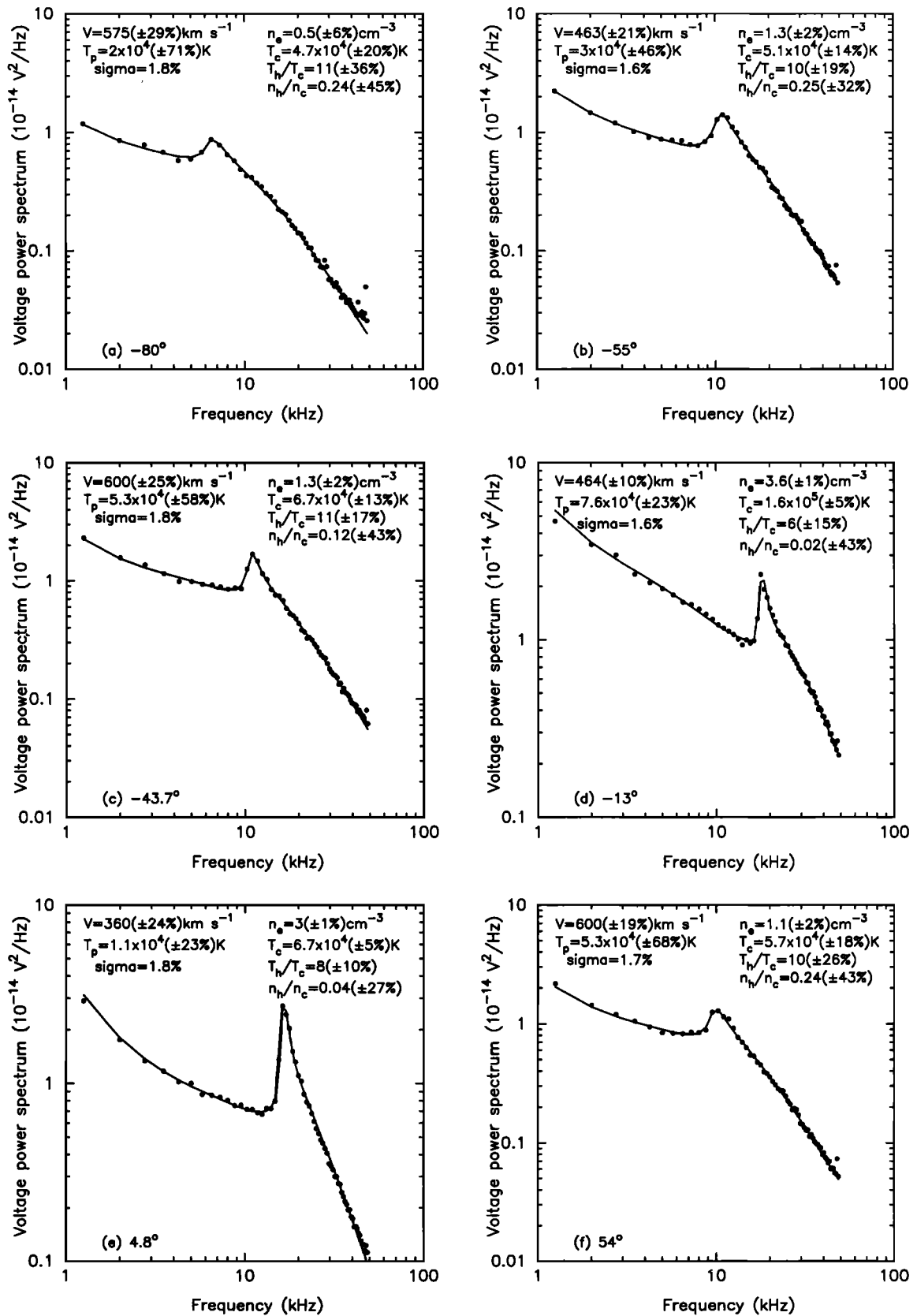


Figure 6. Series of typical voltage power spectra (in $10^{-14} \text{ V}^2 \text{ Hz}^{-1}$) measured with the URAP dipole antenna on Ulysses at various distances and at latitudes of (a) -80° , (b) -55° , (c) -43.7° , (d) -13° , (e) 4.8° , and (f) 54° . Solid lines are the best fits to the data (dots), with the plasma parameters shown.

wind speed, the core temperature, and the proton temperature are determined from the low-frequency part of the spectrum with a reduced number of data points, which implies larger numerical uncertainties on them.

Generally, the solar wind speed is deduced with an accuracy of 10-30%, with a better accuracy for slow solar wind speed, as said above. We obtain the total electron density with a few percent since it is mainly derived from the measurement of a frequency and is thus independent of the receiver gain calibration. A good accuracy is also achieved for the core temperature T_c , which has an uncertainty smaller than 10% for in-ecliptic measurements and lower than 25% poleward of 40° . Notice that the QTN method allows us to obtain a better accuracy on the derived electron temperature T_e than when the drift velocity was not included in the QTN theory [Meyer-Vernet *et al.*, 1998].

4. Comparison With Particle Analyser on Ulysses

Since the wire dipole antenna senses a large plasma volume, the QTN spectroscopy method is relatively immune to spacecraft potential and photoelectron perturbations [Meyer-Vernet *et al.*, 1998]. Indeed, since the Langmuir wavelength satisfies the inequality $\lambda_L > 2\pi L$ the antenna can be seen as a sensor of surface $S > 2\pi L_D \times L$, which is much larger than the spacecraft scales, including the photoelectron sheath. Moreover, as already said, the total density measurement is independent of the receiver gain calibration.

The plasma QTN diagnostic on Ulysses is made every 128 s, at twice the rate of the Solar Wind Observations Over the Poles of the Sun (SWOOPS) particle analyser [Bame *et al.*, 1992] on board. This high time resolution is important to study the solar wind fluctuations. It has allowed the first accurate measurement of the electron density and core temperature radial profiles in the steady state fast solar wind, during the Ulysses high-latitude exploration [Issautier *et al.*, 1998]. However, the frequency resolution is not as good as we wish; the spectrum peak is generally defined by three consecutive frequencies acquired in 6 s, so that the plasma density fluctuations can broaden the spectral peak and limit the accuracy on the measurements of the suprathermal parameters [Meyer-Vernet and Perche, 1989]. Let us now compare some examples of QTN measurements with those deduced from the SWOOPS particle analyser on Ulysses.

Figure 7 represents the electron density, the core electron temperature, and the solar wind speed, deduced from the present extended QTN method, compared with the SWOOPS data, in the latitudinal range (-30° S, $+30^\circ$ N), during the Ulysses fast latitude transit near the 1996 solar activity minimum. In Figure 7 one can see the abrupt change of regime near $\pm 22^\circ$ between the heliographic current sheet and the polar regions. In the top plot, one can also point out that the total electron density deduced from QTN superimposes very well to the total ion density deduced from the proton density plus twice the alpha particle density, obtained with the SWOOPS experiment, yielding indistinguishable

values at the scale of Figure 7. However, the SWOOPS total electron densities (not shown) are not in agreement with the present QTN densities, both in the high and slow speed wind, owing to potential perturbations which affect classical electron analyser.

The middle plot of Figure 7 shows that the core electron temperature obtained by the QTN method is rather close to the SWOOPS results, in the dense equatorial band as well as at high latitudes. Actually, SWOOPS core temperature measurements are, on average, higher to within 12% than the QTN ones, while these two measurements are closer to each other outside the heliospheric current sheet.

Finally, the comparison of the solar wind speed measured by the two methods (QTN and SWOOPS), in the bottom plot, shows quite a good agreement, generally better than 10%, for low to medium solar wind speeds in the equatorial band where the speed varies between 300 and 650 km s^{-1} . However, the QTN speed data are systematically lower by 25% than SWOOPS data at high latitudes are, where the solar wind speed is large and remains near 750 km s^{-1} . Note that the SWOOPS experiment [Scime *et al.*, 1994] gives the solar wind speed with a few percent uncertainty because its diagnostic is based on the shift of the proton velocity distribution.

5. Discussion and Summary

How can we explain this lack of accuracy of the QTN speed measurements at high latitudes? It may be due to the fact that we did not take into account the solar wind speed effect on the electrons. Indeed, in slow solar wind ($\sim 400 \text{ km s}^{-1}$) the assumption $V \ll v_{the}$ is well satisfied, so that the effect of the bulk speed can be neglected for the electron thermal noise. In contrast, for large-speed wind this inequality is less well satisfied since, as noted in section 2.4.2, we have $V/v_{the} \sim 0.6$. In addition, for this large-speed value, the Doppler shift of f_p discussed in section 2.4.2 should widen the peak, thereby producing an overestimation of the parameter α , which is determined from the width of the spectral peak. This is actually what is observed, and the overestimation of α may, in turn, affect the speed measurement. Indeed, we checked that in these cases; using a realistic value of α reduces the discrepancy on the speed measurement. Notice that, in contrast, for slow speed wind, both α and V agree with the SWOOPS particle analyser data better than 10%. This suggests that further calculations are needed to improve the bulk solar wind speed determination in this case.

Finally, the proton temperature is not well measured since the proton thermal noise is not very sensitive to T_p (see equation (22)). Note also that the velocity distributions in the high-speed wind are not well described by a superposition of isotropic Maxwellians [Feldman *et al.*, 1996]. The temperature anisotropy is not expected to affect significantly the thermal noise spectroscopy for electrons [Meyer-Vernet, 1994], but this is not necessarily true for the proton thermal noise. This effect may affect the determina-

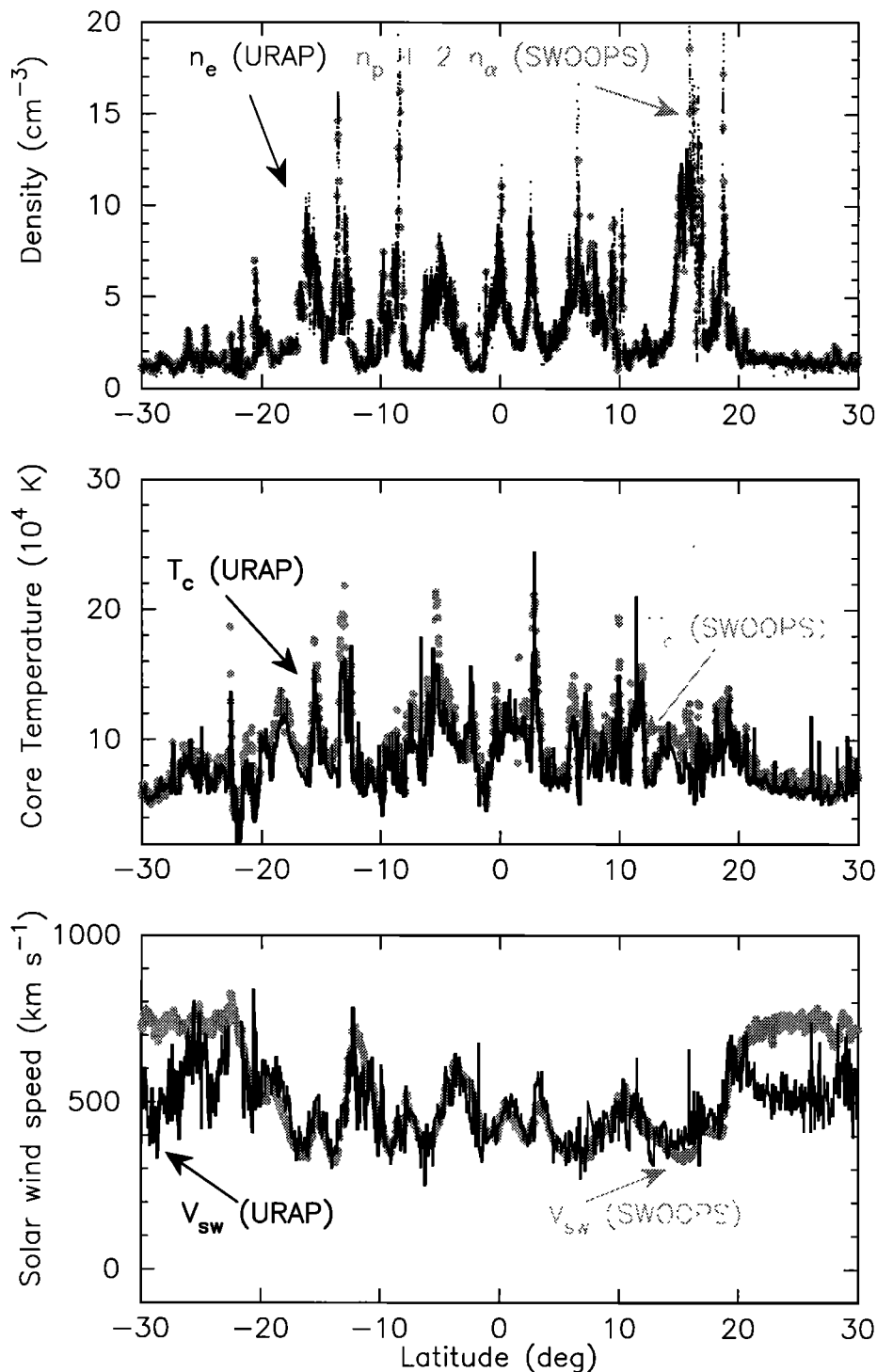


Figure 7. Comparison of the density, thermal temperature, and solar wind speed, deduced from the QTN extended method (continuous line) and from the particle analyser experiment (grey dots) SWOOPS (Solar Wind Observations Over the Poles of the Sun) on Ulysses. Note that both measurements are hourly averaged.

tion of the fast solar wind speed. Anyway, the present extended QTN method significantly improves the precision on the core temperature diagnostic even when only an order of magnitude of the fast wind speed is derived.

Finally, in this paper, we have extended the method of quasi-thermal noise spectroscopy to take into account the Doppler-shifted proton contribution to deduce the solar wind

speed and to improve the diagnostic of the electron core temperature. It is noteworthy that since we consider only waves at frequencies of the order of magnitude of the plasma frequency, neglecting the ambient magnetic field requires the electron gyrofrequency to be much smaller than the plasma frequency. This is the case in our study since Ulysses solar wind measurements are obtained between 1 and 4 AU, where

the magnetic field is about 5×10^{-9} T and the electron gyro-frequency is about 0.9 kHz. Analytical expressions of the proton thermal noise are given in section 2, and its contour levels are represented as functions of the electron density and temperature; they can be readily used to estimate the proton thermal noise at the ports of electric antennae in nonmagnetized plasmas, in addition to the electron contribution which has been developed by *Meyer-Vernet and Perche* [1989].

The quasi-thermal noise method, generalized to a drifting plasma in the present paper, provides an accurate determination of the solar wind plasma. It is complementary to classical particle analysers for both interplanetary, planetary, and cometary environment studies, and it can be used to cross-check other instruments. It is planned to be also used on several spacecraft to measure the electron density and temperature, in particular, on Cassini in the ionosphere of Venus, in the inner magnetosphere of Saturn, and on the Imager for Magnetopause-to-Aurora Global Exploration (IMAGE) mission in the Earth's magnetosphere.

Appendix: Kramers-Kronig Relations

The analyticity of the function $\epsilon_L(k, \omega)$ in the upper half angular frequency ω plane allows the use of the Cauchy's theorem to relate the real and imaginary parts of $\epsilon_L(k, \omega)$ on the real axis and to deduce the Kramers-Kronig relation [Jackson, 1975]. Let z be a point inside a closed contour C in the ω plane; then a given function having the same analyticity property of $\epsilon_L(k, z)$ is given using Cauchy's theorem by

$$f(k, z) = \frac{1}{2\pi i} \oint_C \frac{f(k, \omega')}{\omega' - z} d\omega' \quad (A1)$$

We now choose the contour C to consist of the real ω axis and a large semicircle in the upper half plane. If $f(k, \omega) - 1$ vanishes sufficiently rapidly at infinity, there is no contribution to the integral from the large semicircle. Thus (A1) can be rewritten as

$$f(k, z) = \frac{1}{2\pi i} \int_{-\infty}^{+\infty} \frac{f(k, \omega')}{\omega' - z} d\omega' \quad (A2)$$

where z is any point in the upper half plane. Taking $z = \omega + i0$ and $\omega = 0$, the real part of the equation is

$$\Re[f(k, 0)] = \frac{1}{\pi} P \int_{-\infty}^{+\infty} \frac{\Im[f(k, \omega')]}{\omega'} d\omega' \quad (A3)$$

where P is the principal part. We now apply this relation to the function $f(k, \omega) = 1/\epsilon_L(k, \omega) - 1$, which vanishes as ω tends to infinity.

Then we derive from (A3)

$$\int_{-\infty}^{+\infty} \frac{d\omega'}{\omega'} \Im \left(\frac{1}{\epsilon_L(k, \omega')} \right) = \pi \Re \left[\frac{1}{\epsilon_L(k, 0)} - 1 \right] \quad (A4)$$

Acknowledgments. The Ulysses URAP investigation is a collaboration of NASA/GSFC, Observatoire de Paris-Meudon, University of Minnesota, and CETP, Velizy, France. The French con-

tribution is supported by CNES and CNRS. Work at Los Alamos was carried out under the auspices of the United States Department of Energy with support from NASA.

Michel Blanc thanks both referees for their assistance in evaluating this paper.

References

- Bame, S. J., et al., The Ulysses solar wind plasma experiment, *Astron. Astrophys. Suppl. Ser.*, **92**, 237, 1992.
- Chateau, Y. F., and N. Meyer-Vernet, Electrostatic noise in non-Maxwellian plasmas: Generic properties and "kappa" distributions, *J. Geophys. Res.*, **96**, 5825, 1991.
- Couturier, P., S. Hoang, N. Meyer-Vernet, and J.-L. Steinberg, Measurements and interpretation of the quasi-thermal noise spectrum in the solar wind: Solar Wind Five, *NASA Conf. Publ.*, **CP-2280**, 377, 1983.
- Feldman, W. C., J. R. Asbridge, S. J. Bame, M. D. Montgomery, and S. P. Gary, Solar wind electrons, *J. Geophys. Res.*, **80**, 4181, 1975.
- Feldman, W. C., B. L. Barraclough, J. L. Phillips, and Y.-M. Wang, Constraints on high-speed solar wind structure near coronal base: A Ulysses perspective, *Astron. Astrophys.*, **316**, 355, 1996.
- Hoang, S., J.-L. Steinberg, P. Couturier, and W. C. Feldman, An electric noise component with density f^{-1} identified on ISEE 3, *J. Geophys. Res.*, **87**, 9025, 1982.
- Hoang, S., et al., Solar wind thermal electrons in the ecliptic plane between 1 and 4AU: Preliminary results from the Ulysses radio receiver, *Geophys. Res. Lett.*, **19**, 1295, 1992.
- Hoang, S., N. Meyer-Vernet, K. Issautier, M. Maksimovic, and M. Moncuquet, Latitudinal dependence of solar wind plasma thermal noise: Ulysses radio observations, *Astron. Astrophys.*, **316**, 430, 1996.
- Issautier, K., N. Meyer-Vernet, M. Moncuquet, and S. Hoang, A novel method to measure the solar wind speed, *Geophys. Res. Lett.*, **23**, 1649, 1996.
- Issautier, K., N. Meyer-Vernet, M. Moncuquet, and S. Hoang, Solar wind radial and latitudinal structure: Electron density and core temperature from Ulysses thermal noise spectroscopy, *J. Geophys. Res.*, **103**, 1969, 1998.
- Jackson, J. D., *Classical Electrodynamics*, 2nd ed., Univ. of Calif. Press, Berkeley, 1975.
- Maksimovic, M., S. Hoang, N. Meyer-Vernet, M. Moncuquet, J.-L. Bougeret, J. L. Phillips, and P. Canu, The solar wind electron parameters from quasi-thermal noise spectroscopy and comparison with other measurements on Ulysses, *J. Geophys. Res.*, **100**, 19881, 1995.
- Maksimovic, M., V. Pierrard, and P. Riley, Ulysses electron distributions fitted with Kappa functions, *Geophys. Res. Lett.*, **24**, 1151, 1997.
- Meyer-Vernet, N., On natural noises detected by antennae in plasmas, *J. Geophys. Res.*, **84**, 5373, 1979.
- Meyer-Vernet, N., On the thermal noise "temperature" in an anisotropic plasma, *Geophys. Res. Lett.*, **21**, 397, 1994.
- Meyer-Vernet, N., and C. Perche, Tool kit for antennae and thermal noise near the plasma frequency, *J. Geophys. Res.*, **94**, 2405, 1989.
- Meyer-Vernet, N., P. Couturier, S. Hoang, J.-L. Steinberg, and R. D. Zwickl, Ion thermal noise in the solar wind: Interpretation of the "excess" electric noise on ISEE 3, *J. Geophys. Res.*, **91**, 3294, 1986.
- Meyer-Vernet, N., S. Hoang, and M. Moncuquet, Bernstein waves in the Io torus plasma: A novel kind of electron temperature sensor, *J. Geophys. Res.*, **98**, 21163, 1993.
- Meyer-Vernet, N., S. Hoang, K. Issautier, M. Maksimovic, R. Manning, M. Moncuquet, and R. G. Stone, Measuring plasma parameters with thermal noise spectroscopy, in *Measurement Techniques in Space Plasmas: Fields*, *Geophys. Monogr. Ser.*, Vol.103, edited by Robert F. Pfaff, J. Borovsky, and David T. Young, pp.205-210, AGU, Washington, D.C., 1998.

- Moncuquet, M., N. Meyer-Vernet, and S. Hoang, Dispersion of electrostatic waves in the IO plasma torus and derived electron temperature, *J. Geophys. Res.*, *100*, 21697, 1995.
- Press, W. H., S. A. Teukolsky, W. T. Vetterling, and B. P. Flannery, *Numerical Recipes*, 2nd ed., Cambridge Univ. Press, New York, 1992.
- Rostoker, N., Fluctuations of a plasma, *Nucl. Fusion*, *1*, 101, 1961.
- Schiff, M. L., Current distribution on a grid type dipole antenna immersed in a warm isotropic plasma, *Radio Sci.*, *6*, 665, 1971.
- Scime, E. E., J. L. Phillips, and S. J. Bame, Effects of spacecraft potential on three-dimensional electron measurements in the solar wind, *J. Geophys. Res.*, *99*, 14769, 1994.
- Sitenko, A. G., *Electromagnetic Fluctuations in Plasma*, Academic, San Diego, Calif., 1967.
- Stone, R. G., et al., The unified radio and plasma wave investigation on Ulysses, *Astron. Astrophys. Suppl. Ser.*, *92*, 291, 1992.
-
- S. Hoang, K. Issautier, N. Meyer-Vernet, and M. Moncuquet, DESPA, CNRS URA 264, Observatoire de Paris, 5 place Jules Janssen, 92195 Meudon, France. (sang.hoang@obspm.fr; karine.issautier@obspm.fr; nicole.meyer@obspm.fr; michel.moncuquet@obspm.fr)
- D. J. McComas, Mail Stop D466, Los Alamos National Laboratory, Los Alamos, NM 87545 (dmccomas@lanl.gov)

(Received September 9, 1998; revised November 26, 1998; accepted December 3, 1998.)